International Journal of Mechanical Sciences 281 (2024) 109503

Contents lists available at ScienceDirect

International Journal of Mechanical Sciences

journal homepage: www.elsevier.com/locate/ijmecsci

Topological bound modes in phononic lattices with nonlocal interactions

V.F. Dal Poggetto [a,*], R.K. Pal [b], N.M. Pugno [c,d], M. Miniaci [a,*]

[a] Univ. Lille, CNRS, Centrale Lille, Junia, Univ. Polytechnique Hauts-de-France, UMR 8520 - IEMN - Institut d'Electronique de Microélectronique et de Nanotechnologie, F-59000 Lille, France

[b] Department of Mechanical and Nuclear Engineering, Kansas State University, Manhattan, KS 66506, USA

[c] Laboratory for Bio-inspired, Bionic, Nano, Meta Materials & Mechanics, Department of Civil, Environmental and Mechanical Engineering, University of Trento, 38123 Trento, Italy

[d] School of Engineering and Materials Science, Queen Mary University of London, Mile End Road, London E1 4NS, United Kingdom

ARTICLE INFO

Keywords:
Elastic waves
Acoustic waveguides
Phononic crystals
Topological mechanics
Bound modes
Localized state

ABSTRACT

Topological protection has opened new possibilities for unconventional wave guiding, object cloaking, improved energy transport, as well as surface, edge, or corner mode localization. In elasticity, these phenomena have largely been explored and exemplified through discrete models having nearest neighbor couplings. Interactions beyond the nearest neighbors in one-dimensional studies, on the other hand, have recently shown great potential for topological wave phenomena.

In this work we investigate the topological modes of a two-dimensional mass–spring hexagonal lattice with connections between both nearest and third nearest neighboring masses. We show that non-nearest connections allow for (i) the formation of additional Dirac cones and (ii) a migration in their location in the reciprocal space as a function of the relative stiffness between nearest and third nearest neighbor connections. These additional Dirac cones are linked to a corresponding increase in the number of topological edge modes, which hybridize and result in bound modes at interfaces between lattices that are inverted copies of each other. Explicit expressions for the mode shapes and frequencies of these bound modes are derived and their topological origin is elucidated. We also demonstrate that by varying the relative stiffness between nearest and third nearest neighbor connections, bound modes lying in the band gap can be achieved. While in the case of only nearest neighbor connections the bound modes are at a fixed frequency in the pass band, varying the stiffness of a single nonlocal spring can shift their frequency and isolate them as desired within a band gap. Transient numerical simulations conducted on a finite lattice allow to quantify the confinement along the transverse direction as a wave propagates in a waveguide with sharp turns, reporting negligible backscattering. Finally, a possible realization of hexagonal unit cells with third nearest neighbor connections is proposed.

The concepts here presented open novel avenues for topological wave guiding and confinement leveraging bound modes to design waveguides with superior energy localization potential.

1. Introduction

The study of wave localization has attracted the interest of researchers for a long time across different domains, from optics to microwaves, electromagnetism, acoustics, and elasticity [1–5]. In the last decade, this field gained a renewed interest thanks to the introduction of the concept of topological protection [6,7], which paved the way towards unconventional wave guiding [8], object cloaking [9], improved energy transport and harvesting [10], as well as surface, edge, or corner mode localization [11,12]. Topological protection guarantees wave confinement (or guiding) through symmetry and topology properties of dispersion surfaces, even in the presence of structural perturbations, such as geometrical and material changes or disorders [13,14]. Originally proposed in the field of quantum mechanics [15], topological protection has successively inspired the quest for its analogue in other research domains, including elastodynamics, where, however, Poisson's effect and both the presence and hybridization of longitudinal and shear waves made the parallel harder to be obtained [16–19]. In particular, elastic metamaterials, i.e., structured materials that exhibit unconventional wave-controlling properties [20–23], have been used as prompt candidates for the aforementioned quest [24–26].

In elasticity, topological protection can be achieved (i) by breaking the time-reversal symmetry using active components, like rotating gyroscopes [27,28] or active fluids [29], or (ii) via solely passive components, requiring only the spatial symmetry of the unit cell to

* Corresponding authors.
E-mail addresses: vinicius.fonseca-dal-poggetto@univ-lille.fr (V.F. Dal Poggetto), marco.miniaci@univ-lille.fr, marco.miniaci@gmail.com (M. Miniaci).

https://doi.org/10.1016/j.ijmecsci.2024.109503
Received 6 April 2024; Received in revised form 2 June 2024; Accepted 21 June 2024
Available online 8 July 2024

be broken [30,31]. In the latter case, which is the focus of this paper, lattices of masses and springs are an ideal playground to explore the aforementioned analogues [32,33].

In this context, Süsstrunk and Huber realized the mechanical analogue of the quantum spin Hall effect [34–37] via a double pendulum array with sophisticated connections, observing the propagation of waves along edges and their immunity to back-scattering at sharp corners [38]. Pal et al. proposed a theoretical framework to achieve elastic helical edge modes by connecting two identical hexagonal mass–spring lattices through inter-layer couplings that broke the double Dirac cone degeneracy [39]. Considering the quantum valley Hall effect [40–43], the requirement of nontrivial topology of the band structure can be relaxed and pursued only in correspondence with the valleys at the high symmetry points of the reciprocal lattice. This may lead to a reduction of the unit cell complexity, but at the same time to a less robust protection due to potential inter-valley scattering. Vila et al. observed topologically protected valley edge waves in an elastic hexagonal lattice adding unequal masses at the hexagon vertices [44], while Pal and Ruzzenne reported this effect in a plate-like structure with a hexagonal arrangement of spring–mass resonators [45], and Chen et al. predicted such phenomena by arranging masses and springs into a Kagome-like lattice [46]. Zhou et al. explored the variation of the inter- and intra-unit cell spring constants to tune and invert the band structure in a hexagonal lattice [47], while Chen et al. analytically explored the potential of gathering all the aforementioned elastic topological analogues into a unified mass–spring honeycomb lattice [48]. An et al. showed how to selectively activate the localization of waves at corners by engineering the positions of the valleys in the dispersion diagram [49].

Finally, another category of localized modes, accidental or symmetry-protected, referred to as bound modes in literature [50–53], has emerged in the field of elasticity in recent years. Bound modes are ideally capable of perfect wave confinement, i.e., achieving a wave amplitude that decays to zero in an extremely compact spatial region, regardless if they reside within a band gap or a pass-band [54], thus yielding extremely high quality factors. Rahman and Pal introduced a rationale to induce bound modes in a one-dimensional mass–spring system by adding defects exploiting reflection symmetry [55]. Their existence has been successively observed in a slender beam with rigid masses attached at periodic intervals. A bounded compact segment with four additional protruding side beams nullifies the forces and moments outside the target region [56]. Other notable works include the observation of bound modes at the edges of elastic plates for waves incident at a specific angle [57,58], whereas Haq et al. proposed an elastic structure made of thin (sub-wavelength) cylindrical scatterers embedded in a background material and arranged into a doubly periodic array [59].

Most of the aforementioned wave phenomena have been explored and exemplified through discrete models accounting for each mass to interact with the nearest neighboring mass. However, interactions beyond the nearest neighbors present great potential for richer topological mechanics. Accounting for non-nearest neighboring interaction of masses has allowed the observation of roton-like dispersion relations in elasticity [60–63], as well as to go beyond the conventional winding numbers in one-dimensional topologically protected mass–spring chains [46]. The existence of multiple localized modes with a topological origin, identified by the number of Dirac points in the Brillouin zone, has been reported recently [64]. Grundmann theoretically analyzed the evolution of topological effects arising from the interaction of masses located at the nearest, second nearest, and third nearest neighbor in diatomic linear elastic chains, reporting two topologically distinct modes by varying the spring constants when only the nearest neighboring masses were connected. No substantial topological changes occurred when the next-nearest neighboring masses were coupled through additional springs, whereas two additional distinct topological modes were observed when coupling the third nearest masses [65]. Betancur-Ocampo et al. predicted, theoretically and numerically, that connecting third nearest neighboring masses can induce topological phase transitions in one-dimensional lattices [66]. Finally, Wang and Wang have proposed active methods to control elastic wave propagation by manipulating topological modes considering nonlocal interactions [67,68], using both numerical calculations and experiments.

Apart from pioneering studies limited to one-dimensional cases, when a two-dimensional lattice is concerned, most of the works currently available in the literature are limited to mass–spring systems where only the nearest neighboring interaction of the masses is considered. To address this gap, we investigate the topological models of a mass–spring hexagonal lattice with springs connecting both the nearest and third nearest neighboring masses. We demonstrate the possibility of forming multiple Dirac cones traversing the reciprocal lattice as the relative stiffness between the two sets of springs (connecting the nearest and third nearest masses) changes. Then, inversion symmetry is broken in the unit cell considering interfaces between two lattices that are inverted copies of each other. We show that the connection of non-neighboring masses allows for the nucleation and tuning of additional Dirac cones in correspondence with the high symmetry points K (K′) when compared to the case of hexagonal lattices where only neighboring masses are connected. An increase in the number of Dirac cones leads to a corresponding increase in the number of topological edge modes, with these edge modes hybridizing and leading to bound modes when finite strips are considered. Explicit expressions are given for the existence of bound modes at the interface and their topological origin is elucidated. Finally, numerical simulations on a finite lattice are conducted to determine the extent of the confinement along the transverse direction as a wave propagates in a waveguide with sharp turns.

The outline of this paper is as follows. Section 2 describes the discrete lattice and derives its dispersion relations. Section 3 presents the investigation of the topological invariants associated with Dirac cones and singularity points in the reciprocal space. Section 4 describes the derivations concerning the existence of bound modes, while transient numerical simulations considering a finite structure are reported in Section 5. Finally, conclusions are drawn in Section 6.

2. Lattice description and dispersion analysis

The theoretical model used to calculate the dispersion diagrams and wave propagation properties of the considered structures are reported in this section. Fig. 1a shows pairs of unequal masses denoted as m_a (in blue) and m_b (in yellow) arranged into a hexagonal lattice described by the direct vectors $\mathbf{a}_1 = \{a, 0\}^T$ and $\mathbf{a}_2 = \left\{a/2, a\sqrt{3}/2\right\}^T$, where a is the spacing between adjacent unit cells. Each mass presents only one degree of freedom, corresponding to an out-of-plane displacement. The nearest neighboring masses are connected by springs of stiffness k_1 (continuous black line), while third nearest neighboring masses are connected by springs of stiffness k_2 (dashed green, purple, orange, and blue lines). The periodic structure can then be obtained by shifting the unit cell, highlighted by the light blue parallelogram, $\{n_1, n_2\} \in \mathbb{Z}^2$ times in the $\{\mathbf{a}_1, \mathbf{a}_2\}$ directions, respectively.

Denoting $v_p^{(n_1,n_2)}$ as the displacements of mass $p = \{a, b\}$ in the unit cell with integer indices (n_1, n_2), the equilibrium of masses m_a and m_b at the base unit cell $(0, 0)$ yields

$$\begin{aligned} m_a \ddot{v}_a^{(0,0)} &= k_1(v_b^{(0,0)} - v_a^{(0,0)}) + k_1(v_b^{(-1,0)} - v_a^{(0,0)}) + k_1(v_b^{(0,-1)} - v_a^{(0,0)}) \\ &\quad + k_2(v_b^{(-1,-1)} - v_a^{(0,0)}) + k_2(v_b^{(-1,1)} - v_a^{(0,0)}) + k_2(v_b^{(1,-1)} - v_a^{(0,0)}), \\ m_b \ddot{v}_b^{(0,0)} &= k_1(v_a^{(0,0)} - v_b^{(0,0)}) + k_1(v_a^{(1,0)} - v_b^{(0,0)}) + k_1(v_a^{(0,1)} - v_b^{(0,0)}) \\ &\quad + k_2(v_a^{(1,1)} - v_b^{(0,0)}) + k_2(v_a^{(1,-1)} - v_b^{(0,0)}) + k_2(v_a^{(-1,1)} - v_b^{(0,0)}). \end{aligned} \tag{1}$$

Given the periodicity of the lattice, the harmonic displacement $v(\mathbf{r}, t) = e^{-i\omega t} v(\mathbf{r})$ is written as a Bloch solution [69] yielding the spatially periodic relation

$$v(\mathbf{r} + \mathbf{R}, t) = e^{i\mathbf{k}\cdot\mathbf{R}} v(\mathbf{r}, t), \tag{2}$$

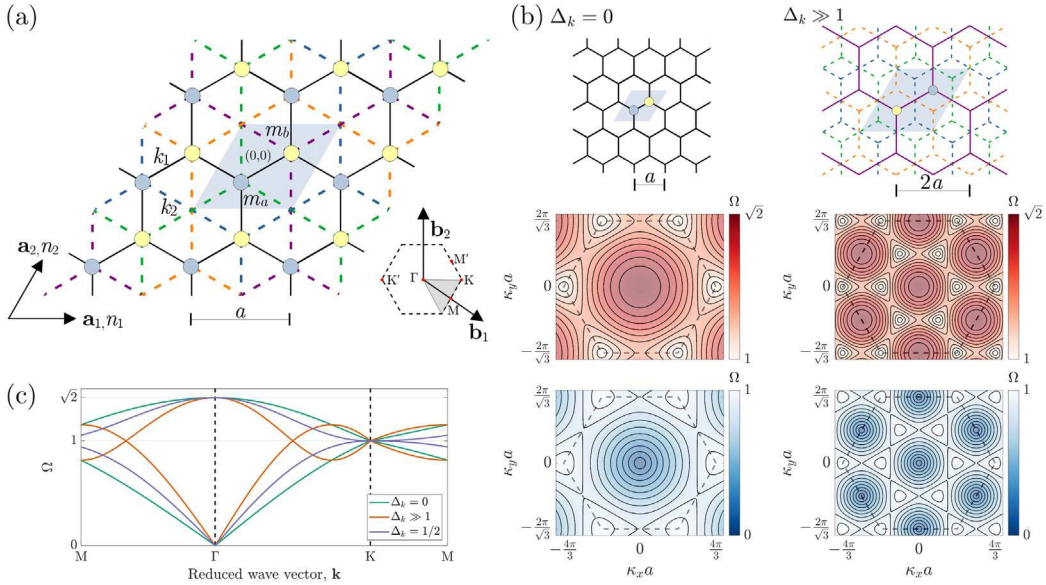

Fig. 1. Discrete elastic lattice and associated dispersion diagrams. (a) Hexagonal lattice described by the lattice vectors $\{\mathbf{a}_1, \mathbf{a}_2\}$, with unit cells with indices (n_1, n_2) and pairs of masses (m_a, m_b) connected to the nearest (third nearest) neighboring masses through springs of stiffness k_1 (k_2) denoted by continuous black (dashed colored) lines. The light blue parallelogram denotes the reference unit cell $(0,0)$. The reciprocal lattice (basis vectors $\{\mathbf{b}_1, \mathbf{b}_2\}$) and high-symmetry points (Γ, K, K′, M, M′) are also shown. (b) Hexagonal lattices (top panels) and dispersion surfaces (middle and bottom panels) for $\Delta_k = 0$ (left panels) and $\Delta_k \gg 1$ (right panels). The unit cells in each case are highlighted in light blue. The lattice for the case $\Delta_k \gg 1$ corresponds to 4 unconnected copies (represented by different colors) of the lattice for the $\Delta_k = 0$ case, with double spacing. One of these 4 lattice is represented in continuous lines (purple) for the sake of clarity. (c) Dispersion curves for $\Delta_k = 0$, $\Delta_k = 1/2$, and $\Delta_k \gg 1$.

$$
\begin{aligned}
\widetilde{\mathbf{K}}_1(\mathbf{k}) &= \begin{bmatrix} 1 & -(1+e^{-i\mathbf{k}\cdot\mathbf{a}_1}+e^{-i\mathbf{k}\cdot\mathbf{a}_2})/3 \\ -(1+e^{i\mathbf{k}\cdot\mathbf{a}_1}+e^{i\mathbf{k}\cdot\mathbf{a}_2})/3 & 1 \end{bmatrix}, \\
\widetilde{\mathbf{K}}_2(\mathbf{k}) &= \begin{bmatrix} 1 & -(e^{i\mathbf{k}\cdot(-\mathbf{a}_1-\mathbf{a}_2)}+e^{i\mathbf{k}\cdot(-\mathbf{a}_1+\mathbf{a}_2)}+e^{i\mathbf{k}\cdot(\mathbf{a}_1-\mathbf{a}_2)})/3 \\ -(e^{i\mathbf{k}\cdot(\mathbf{a}_1+\mathbf{a}_2)}+e^{i\mathbf{k}\cdot(\mathbf{a}_1-\mathbf{a}_2)}+e^{i\mathbf{k}\cdot(-\mathbf{a}_1+\mathbf{a}_2)})/3 & 1 \end{bmatrix}, \\
\mathbf{M} &= \begin{bmatrix} m_a & 0 \\ 0 & m_b \end{bmatrix},
\end{aligned}
\tag{5}
$$

Box I.

where $\mathbf{r}$ and t represent the spatial and time coordinates, respectively, ω the circular frequency, $\mathbf{k}$ the wave vector, and $\mathbf{R}$ a spatial shift in the form $\mathbf{R} = n_1\mathbf{a}_1 + n_2\mathbf{a}_2$. Thus, Eq. (2) can be rewritten as

$$
v^{(n_1,n_2)} = e^{i\mathbf{k}\cdot(n_1\mathbf{a}_1)} e^{i\mathbf{k}\cdot(n_2\mathbf{a}_2)} v^{(0,0)}, \tag{3}
$$

where $v^{(n_1,n_2)} = v(\mathbf{r}+\mathbf{R}, t)$ and $v^{(0,0)} = v(\mathbf{r}, t)$. This allows to directly represent the relation between the masses of the unit cell with coordinates (n_1, n_2) and the base unit cell $(0,0)$.

Combining Eqs. (1)–(3) leads to the eigenproblem

$$
(3k_1\widetilde{\mathbf{K}}_1(\mathbf{k}) + 3k_2\widetilde{\mathbf{K}}_2(\mathbf{k}) - \omega^2\mathbf{M})\mathbf{u} = \mathbf{0}, \tag{4}
$$

with matrices (Eq. (5)) in Box I and $\mathbf{u} = \{u_a, u_b\}^T$, where $u_a = v_a^{(0,0)}$ and $u_b = v_b^{(0,0)}$ have been used for the sake of simplicity.

By imposing a perturbation Δ_m on a reference mass m such that $m_a = m(1+\Delta_m)$ and $m_b = m(1-\Delta_m)$, and denoting $k_2 = k_1\Delta_k$, Eq. (4) is rewritten as

$$
\left(\frac{1}{1+\Delta_k}\widetilde{\mathbf{K}}_1(\mathbf{k}) + \frac{\Delta_k}{1+\Delta_k}\widetilde{\mathbf{K}}_2(\mathbf{k}) - \Omega^2\widetilde{\mathbf{M}}\right)\mathbf{u} = \mathbf{0}, \tag{6}
$$

where $\Omega = \omega/\omega_0$, with $\omega_0 = \sqrt{3(k_1+k_2)/m}$ being a dimensionless frequency, and $\widetilde{\mathbf{M}} = \mathrm{diag}(1+\Delta_m, 1-\Delta_m)$.

The dispersion relation $\Omega = \Omega(\mathbf{k})$ can be calculated by setting the determinant of the matrix in Eq. (6) to zero, obtaining the characteristic equation

$$
\Omega^4(1-\Delta_m^2) - 2\Omega^2 + (1-\varphi(\mathbf{k})) = 0. \tag{7}
$$

Here $\varphi(\mathbf{k})$ is expressed as

$$
\varphi(\mathbf{k}) = \frac{\varphi_1(\mathbf{k}) + \varphi_{12}(\mathbf{k})\Delta_k + \varphi_2(\mathbf{k})\Delta_k^2}{(1+\Delta_k)^2}, \tag{8}
$$

with

$$
\begin{aligned}
\varphi_1(\mathbf{k}) &= (3 + e^{i\mathbf{k}\cdot\mathbf{a}_1} + e^{-i\mathbf{k}\cdot\mathbf{a}_1} + e^{i\mathbf{k}\cdot\mathbf{a}_2} + e^{-i\mathbf{k}\cdot\mathbf{a}_2} + e^{i\mathbf{k}\cdot(\mathbf{a}_1-\mathbf{a}_2)} + e^{-i\mathbf{k}\cdot(\mathbf{a}_1-\mathbf{a}_2)})/9, \\
\varphi_2(\mathbf{k}) &= (3 + e^{i2\mathbf{k}\cdot\mathbf{a}_1} + e^{-i2\mathbf{k}\cdot\mathbf{a}_1} + e^{i2\mathbf{k}\cdot\mathbf{a}_2} + e^{-i2\mathbf{k}\cdot\mathbf{a}_2} + e^{i2\mathbf{k}\cdot(\mathbf{a}_1-\mathbf{a}_2)} \\
&\quad + e^{-i2\mathbf{k}\cdot(\mathbf{a}_1-\mathbf{a}_2)})/9, \\
\varphi_{12}(\mathbf{k}) &= (2(e^{i\mathbf{k}\cdot\mathbf{a}_1} + e^{-i\mathbf{k}\cdot\mathbf{a}_1} + e^{i\mathbf{k}\cdot\mathbf{a}_2} + e^{-i\mathbf{k}\cdot\mathbf{a}_2} + e^{i\mathbf{k}\cdot(\mathbf{a}_1-\mathbf{a}_2)} + e^{-i\mathbf{k}\cdot(\mathbf{a}_1-\mathbf{a}_2)}) \\
&\quad + e^{i\mathbf{k}\cdot(\mathbf{a}_1+\mathbf{a}_2)} + e^{-i\mathbf{k}\cdot(\mathbf{a}_1+\mathbf{a}_2)} + e^{i\mathbf{k}\cdot(2\mathbf{a}_1-\mathbf{a}_2)} + e^{-i\mathbf{k}\cdot(2\mathbf{a}_1-\mathbf{a}_2)} \\
&\quad + e^{i\mathbf{k}\cdot(-\mathbf{a}_1+2\mathbf{a}_2)} + e^{-i\mathbf{k}\cdot(-\mathbf{a}_1+2\mathbf{a}_2)})/9.
\end{aligned}
\tag{9}
$$

We remark here that $\varphi_1(\mathbf{k}) > 0$ for $\mathbf{k} \in \mathbb{R}^2$, $\varphi_2(\mathbf{k}) > 0$ for $\mathbf{k} \in \mathbb{R}^2$, and $-2/3 < \varphi_{12}(\mathbf{k}) < 2$ for $\mathbf{k} \in \mathbb{R}^2$. Note that the expression for $\varphi(\mathbf{k})$ remains invariant under the transformation $\mathbf{k} \to \mathbf{R}_{\pi/3}\mathbf{k}$, where $\mathbf{R}_\theta$ is a rotation matrix that rotates vectors by an angle θ, i.e., when the wave vector is rotated by $\pi/3$ about the Γ point. Hence the set of zeros of $\varphi(\mathbf{k})$ has 6-fold rotation symmetry about the origin. In addition, $\varphi(\mathbf{k})$

has 3-fold rotation symmetry about each K point (see Appendix A for further details).

The solution of Eq. (7) yields a pair of dispersion surfaces $\Omega_{1,2}(\mathbf{k})$ given by

$$\Omega^2_{1,2}(\mathbf{k}) = \frac{1}{1-\Delta_m^2} \pm \sqrt{\frac{\varphi(\mathbf{k})}{1-\Delta_m^2} + \left(\frac{\Delta_m}{1-\Delta_m^2}\right)^2}\,. \tag{10}$$

For the particular case of a unit cell with equal masses ($\Delta_m = 0$), it reduces to

$$\Omega^2_{1,2}(\mathbf{k}) = 1 \pm \sqrt{\varphi(\mathbf{k})}\,. \tag{11}$$

The dispersion surfaces, thus, exhibit Dirac cones (i.e., $\Omega_1(\mathbf{k}) = \Omega_2(\mathbf{k})$) at the solutions of $\varphi(\mathbf{k}) = 0$. In the case of unit cells with distinct masses ($\Delta_m \neq 0$), the degeneracy of frequencies at the Dirac cones disappears and a band gap opens. The normalized frequency band width is given by

$$\Omega_2 - \Omega_1 = \frac{1}{\sqrt{1-\Delta_m}} - \frac{1}{\sqrt{1+\Delta_m}}\,. \tag{12}$$

When only nearest neighboring masses are connected ($\Delta_k = 0$) the dispersion relation simplifies, since $\varphi(\mathbf{k}) = \varphi_1(\mathbf{k})$, and the unit cell reduces to the one shown in the top left panel of Fig. 1b. Rewriting the wave vector as $\mathbf{k} = \kappa_1\mathbf{b}_1 + \kappa_2\mathbf{b}_2$, with $\mathbf{b}_1 = \left\{2\pi/a,\, -2\pi/a\sqrt{3}\right\}^T$ and $\mathbf{b}_2 = \left\{0,\, 4\pi/a\sqrt{3}\right\}^T$ being the reciprocal lattice vectors [70], φ_1 can be expressed as

$$\varphi_1(\kappa_1,\kappa_2) = (3+e^{\mathrm{i}\kappa_1 2\pi}+e^{-\mathrm{i}\kappa_1 2\pi}+e^{\mathrm{i}\kappa_2 2\pi}+e^{-\mathrm{i}\kappa_2 2\pi}+e^{\mathrm{i}(\kappa_1-\kappa_2)2\pi}+e^{-\mathrm{i}(\kappa_1-\kappa_2)2\pi})/9\,. \tag{13}$$

Eq. (13) presents solutions $\varphi_1(\kappa_1,\kappa_2) = 0$ for the $\{\kappa_1, \kappa_2\}$ pairs $\{\pm 2/3, \pm 1/3\}$, $\{\pm 1/3, \pm 2/3\}$, $\{\pm 1/3, \mp 1/3\}$, corresponding to the K and K′ points of the first Brillouin zone [71]. The dispersion surfaces nucleating the six Dirac cones ($\Omega = 1$, contour plot going to white) are displayed in the middle and lower left panels of Fig. 1b.

When the connections of third nearest neighboring masses are predominant ($\Delta_k \gg 1$), the characteristic equation is also simplified, since $\varphi(\mathbf{k}) \approx \varphi_2(\mathbf{k})$. The dispersion surfaces are similar to those of the previous case (when $\Delta_k = 0$) but with a double lattice length ($2a$), since $\varphi_2(\mathbf{k}) = \varphi_1(2\mathbf{k})$. This condition results in a lattice equivalent to 4 unconnected copies of the $\Delta_k = 0$ lattice, as represented in the top right panel of Fig. 1b, where the unconnected hexagons are represented by different dashed colored lines. The local linear energy dispersion at the vicinity of the K-points are equivalent to the previous case ($\Delta_k = 0$), as represented by the middle and lower right panels of Fig. 1b.

The case $0 < \Delta_k < 1$ represents the possibility of tuning the dispersion surfaces using the stiffness ratio of springs connecting the nearest and third nearest neighboring masses. The dispersion curves along the M-Γ-K-M path of the first Brillouin zone are illustrated in Fig. 1c for the cases $\Delta_k = 0$, $\Delta_k = 1$, and $\Delta_k = 1/2$ (see Appendix B for further details on the choice of these values).

3. Trajectories of Dirac cones and topological invariants

The high symmetry points K and K′ host Dirac cones for the hexagonal lattice for all values of $\Delta_k \geq 0$ (see Fig. 1b). The loci of the Dirac cones for different values of the stiffness ratio Δ_k are given by the solutions of $\varphi(\mathbf{k}) = 0$ (see Eq. (11)). A direct substitution shows that $\varphi(\mathbf{k}) = 0$ for all values of $\Delta_k \geq 0$ at the K point of coordinates $(4\pi/3a, 0)$, as indicated by the vertical blue line in Fig. 2a, reporting the trajectories of Dirac cones in the (κ_x, Δ_k) plane at $\kappa_y = 0$. The location of this cone does not vary as a function of Δ_k. For $\Delta_k = 1/3$, an additional Dirac cone, reported in red and denoted as (i), arises at the high symmetry M point of coordinates $(\pi/a, -\pi/a\sqrt{3})$. Further increasing Δ_k, this cone moves to K when $\Delta_k = 1/2$, and then towards K/2 when $\Delta_k > 1/2$, as shown by the portion of the curve denoted as (i′).

The number of additional Dirac cones formed, and their respective trajectories as a function of Δ_k, is numerically derived by solving the equation $\varphi(\mathbf{k}) = 0$ for each Δ_k in a region of $(\frac{2\pi}{3a} \times \frac{2\pi}{a\sqrt{3}})$ size around the K point in the first Brillouin zone (see Fig. 2b). From this analysis it emerges that for $\Delta_k = 1/3$, three additional Dirac cones (red curves), the evolution of which is denoted as (i)-(i′), (ii)-(ii′), and (iii)-(iii′), arise at the high symmetry M points. As Δ_k increases further, the Dirac cones move along the M–K path and intersect at the K point when $\Delta_k = 1/2$, resulting in a four-fold degeneracy. For larger values of Δ_k, these newer Dirac cones move towards the wave vector at K/2 $(2\pi/3a, 0)$, as described by the trajectories (i′), (ii′), and (iii′). It is worth mentioning here that the K/2 point corresponds to the K point in the reciprocal lattice of a larger hexagonal lattice with twice the unit cell length (see the right panel of Fig. 1b). This can be explained by recalling that $\varphi(\mathbf{k}) \to \varphi_2(\mathbf{k})$ as $\Delta_k \gg 1$ and φ_2 is similar to φ_1, with the lattice vectors doubled. Thus, in the limit $\Delta_k \gg 1$, the reciprocal lattice vectors and dispersion surface is a smaller copy, by a factor 2, of the $\Delta_k = 0$ case. The reciprocal lattice symmetries about the Γ and K points allow to determine Dirac points in the entire reciprocal space (Fig. 2c). The curves indicating Dirac cone locations are depicted using two colors (blue and red) corresponding to their opposite Berry phase (see Fig. 2d). An analogous behavior, but with opposite Berry phase, is observed in the K′ points.

In a topological insulator, a non-zero Berry curvature [72–74] around a gap is an indicative of the topological protection of the gap. In this case, the associated topological invariant is the valley Chern number [75], obtained by integrating the Berry curvature in the area surrounding one of the nodal degeneracies observed for $\Delta_m = 0$.

Recalling the eigenproblem given by Eq. (6), i.e., $\left(\frac{1}{1+\Delta_k}\widetilde{\mathbf{K}}_1(\mathbf{k}) + \frac{\Delta_k}{1+\Delta_k}\widetilde{\mathbf{K}}_2(\mathbf{k}) - \Omega^2\widetilde{\mathbf{M}}\right)\mathbf{u} = \mathbf{0}$, the corresponding eigenvalues Ω^2 and eigenvectors $\mathbf{u}$ are computed for each wave vector $\mathbf{k}$, i.e., $\Omega^2 = \Omega^2(\mathbf{k})$ and $\mathbf{u} = \mathbf{u}(\mathbf{k})$. The corresponding Berry flux, which approximates the Berry curvature, can then be determined in a discrete $\mathbf{k}$-space computing the quantity [28]

$$B(\mathbf{k}) = \mathrm{Im}\left(\ln\left(\frac{\langle\mathbf{u}(\mathbf{k}_1)|\mathbf{u}(\mathbf{k}_2)\rangle\langle\mathbf{u}(\mathbf{k}_2)|\mathbf{u}(\mathbf{k}_3)\rangle\langle\mathbf{u}(\mathbf{k}_3)|\mathbf{u}(\mathbf{k}_4)\rangle\langle\mathbf{u}(\mathbf{k}_4)|\mathbf{u}(\mathbf{k}_1)\rangle}{\langle\mathbf{u}(\mathbf{k}_1)|\mathbf{u}(\mathbf{k}_1)\rangle\langle\mathbf{u}(\mathbf{k}_2)|\mathbf{u}(\mathbf{k}_2)\rangle\langle\mathbf{u}(\mathbf{k}_3)|\mathbf{u}(\mathbf{k}_3)\rangle\langle\mathbf{u}(\mathbf{k}_4)|\mathbf{u}(\mathbf{k}_4)\rangle}\right)\right), \tag{14}$$

where $\langle\mathbf{u}(\mathbf{k})|\mathbf{u}(\mathbf{k}')\rangle = \mathbf{u}(\mathbf{k})^H\,\widetilde{\mathbf{M}}\,\mathbf{u}(\mathbf{k}')$, $(\cdot)^H$ denotes a conjugate transpose vector, and the wave vectors $\mathbf{k}_1$, $\mathbf{k}_2$, $\mathbf{k}_3$, and $\mathbf{k}_4$ are defined as $\mathbf{k}_1 = \left\{\kappa_x - d\kappa_x, \kappa_y - d\kappa_y\right\}^T$, $\mathbf{k}_2 = \left\{\kappa_x + d\kappa_x, \kappa_y - d\kappa_y\right\}^T$, $\mathbf{k}_3 = \left\{\kappa_x + d\kappa_x, \kappa_y + d\kappa_y\right\}^T$, and $\mathbf{k}_4 = \left\{\kappa_x - d\kappa_x, \kappa_y + d\kappa_y\right\}^T$, where $d\kappa_x \times d\kappa_y$ corresponds to a small patch in the $\mathbf{k}$-space centered at (κ_x, κ_y). The computed Berry flux values are shown in Fig. 2d for selected values of Δ_k, namely 0, 1/3, 1/2, 1, and $\gg 1$ (see Supplementary Movie 1 for the maps of $B(\mathbf{k})$ at intermediate values of Δ_k). Analogous results are obtained using the Berry curvature formulation presented in [76] and given in Appendix C.

When only nearest neighbor connections are present ($\Delta_k = 0$) Berry flux values of $-\pi$ ($+\pi$) at the K (K′) points are found. As the value of Δ_k increases between 0 and 1/2, regions of opposed phase $+\pi$ ($-\pi$) are formed between the K (K′) and M points (midpoint between K and K′ points, illustrated by $\Delta_k = 1/3$). Once Δ_k reaches the value of 1/2, both K and K′ points present a zero value of Berry flux, with a surrounding region presenting values of $+\pi$ ($-\pi$). For increasing values of $\Delta_k > 1/2$, the peaks of $+\pi$ ($-\pi$) values are dislocated to the center of each Brillouin zone, stabilizing in the form of a reciprocal lattice with a double lattice length ($2a$), corresponding to the only non-nearest neighboring connections case ($\Delta_k \gg 1$).

Thus, the red and blue curves in Fig. 2a–c indicate Dirac cones where the lower dispersion surface has, respectively, positive and negative Berry flux values in their vicinity. As previously mentioned,

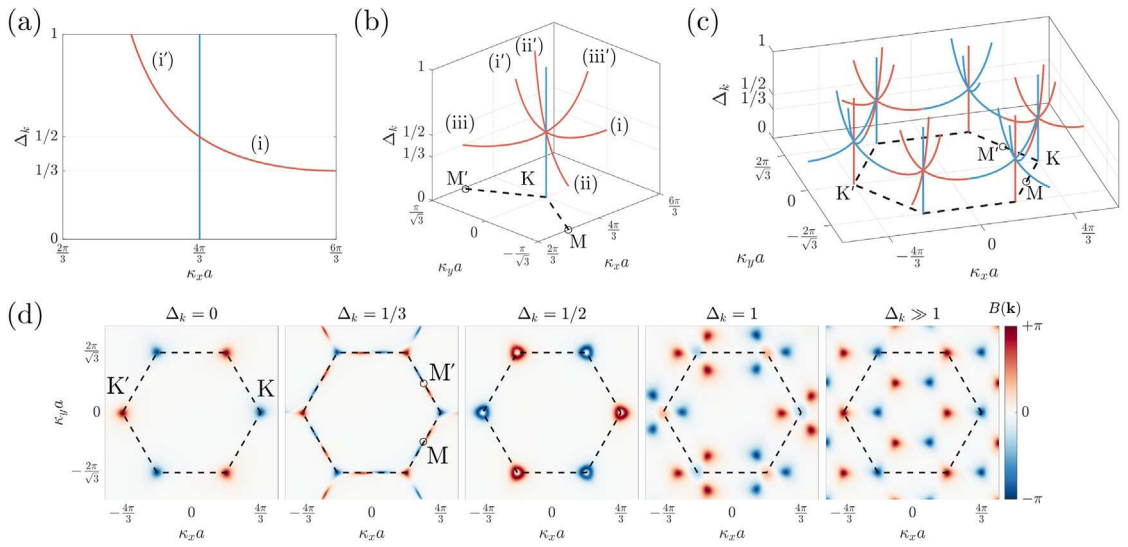

Fig. 2. Loci of the Dirac cones and Berry flux in reciprocal space. (a-c) Location of Dirac cones and their evolution for increasing values of the stiffness ratio Δ_k: (a) representation in the (κ_x, Δ_k) plane at $\kappa_y = 0$, (b) close-up view around the K point for $\kappa_x \in [\frac{2\pi}{3a}, \frac{6\pi}{3a}]$ and $\kappa_y \in [-\frac{\pi}{a\sqrt{3}}, \frac{\pi}{a\sqrt{3}}]$, and (c) Dirac cones in the entire reciprocal space. (d) Berry flux $B(\mathbf{k})$ computed for increasing values of Δ_k.

Dirac cones at K and K′ points have opposite Berry flux values. In addition, the two Dirac cones originating at the M point at $\Delta_k = 1/3$ have opposite signs of Berry flux. The Dirac cones that intersect at each K point all have the same phase, which is opposite to the one at the K′ point. Finally, an inversion in the sign of the Berry flux is obtained exactly at $\Delta_k = 1/2$ in the vicinity of the K (positive) and K′ (negative) points.

The valley Chern number is computed by integrating the Berry flux over the K and K′ points as

$$C_v = \frac{1}{2\pi} \sum_{\kappa_x} \sum_{\kappa_y} B(\mathbf{k}) \,. \tag{15}$$

The computation of C_v using the results presented in Fig. 2d yields the values $-1/2$ and $+1/2$, respectively, for the K and K′ points when $\Delta_k \neq 1/2$. When $\Delta_k < 1/3$, the Berry curvature is zero everywhere except around the K and K′. In this range of Δ_k, a valley Chern number of $\pm 1/2$ indicates the presence of a localized mode at an interface between two lattices that are inverted copies of each other [45]. When $\Delta_k > 1/3$, the Berry curvature is non-zero at other points in the reciprocal lattice, revealing that it does not suffice to examine only the high symmetry K and K′ points. A special case arises at $\Delta_k = 1/2$, when the Dirac cones merge and the Berry flux is concentrated around these high symmetry points. At this Δ_k, the valley Chern numbers are $+1$ and -1 for the K and K′ points, respectively. These values indicate the existence of two localized modes at an interface, similar to that observed in [77] due to the higher valley Chern number. In the next section, we demonstrate how these modes hybridize at the high symmetry point to give rise to bound modes at an interface.

4. Interface modes in a finite strip

In the previous section, we have seen that the connection of non-neighboring masses has allowed for the nucleation and merging of additional Dirac cones at the high symmetry points K (K′). An increase in the number of Dirac cones leads to a corresponding increase in the number of topological edge modes, as recently shown in a one-dimensional mass–spring chain where non-adjacent masses were connected through additional springs [64]. Here, we examine a one-dimensional periodic finite strip obtained by arranging the investigated hexagonal lattice into regions with opposing mass variations. The interface created between such regions allows the leverage of edge modes.

To this purpose, a lattice with an infinite number of unit cells in the $\mathbf{a}_1$-direction and a finite number of unit cells in the $\mathbf{a}_2$-direction, containing an interface between (i) a top region with unit cells with $\Delta_{m,t}$ (recalling that Δ_m is the variation between the two masses of a unit cell) and (ii) a bottom region with unit cells with $\Delta_{m,b} = -\Delta_{m,t}$ is considered. This configuration is presented in Fig. 3a, where the masses are labeled as $1, 2, \ldots, 2n_p$, for n_p pairs of masses in the strip unit cell (dashed parallelogram) and the interface indicated using a red dashed line. The dispersion relations for different values of Δ_k in this strip are computed by imposing periodicity condition on its left and right boundaries (the derivation is presented in Appendix D).

Fig. 3b (top left panel) shows the dispersion diagram for the case of only nearest neighboring masses connected (i.e., $\Delta_k = 0$). The curves are reported for $n_p = 20$ and $\Delta_m = 1/5$. Similar results are obtained when different values of n_p and Δ_m are considered (see Supplementary Movie 3). The dispersion curves shown in black indicate bulk (globally spanning) modes, whereas the two branches enveloping the ensemble of curves located between $1 < \Omega < \sqrt{2}$ (highlighted in green and red) are localized at the interface. The wave modes corresponding to these branches are shown in the bottom left panel of Fig. 3b (green and red stars, respectively), reported at $\kappa_x = 0$. Note that these modes present, respectively, even and odd symmetries with respect to the interface (red dashed line). These symmetries are lost with respect to the interface at the high symmetry point X ($\kappa_x = \pi/a$) because subsequent pairs of masses are fully decoupled (top right panel of Fig. 3b). Due to the full decoupling of adjacent pairs of masses, both even (green) and odd (red) branches converge to the same propagating frequency, whose associated wave modes represent an ideal condition of localization of displacements, as represented by the wave modes shown under the yellow circle symbol (bottom right panel of Fig. 3b). We remark, however, that these correspond to bound modes in the continuum (i.e., frequencies within the range of the bulk bands) and cannot be excited in an isolated manner due to the frequency coincidence with the bulk modes.

The symmetry conditions for the decoupling of adjacent pairs of masses in the finite strip has been reported in literature (see Fig. 21b in [31]) and it can be explained as follows (refer to Appendix D for the full derivation). Imposing the condition of Bloch periodicity and noting that the displacements are exactly out-of-phase in adjacent unit cells at

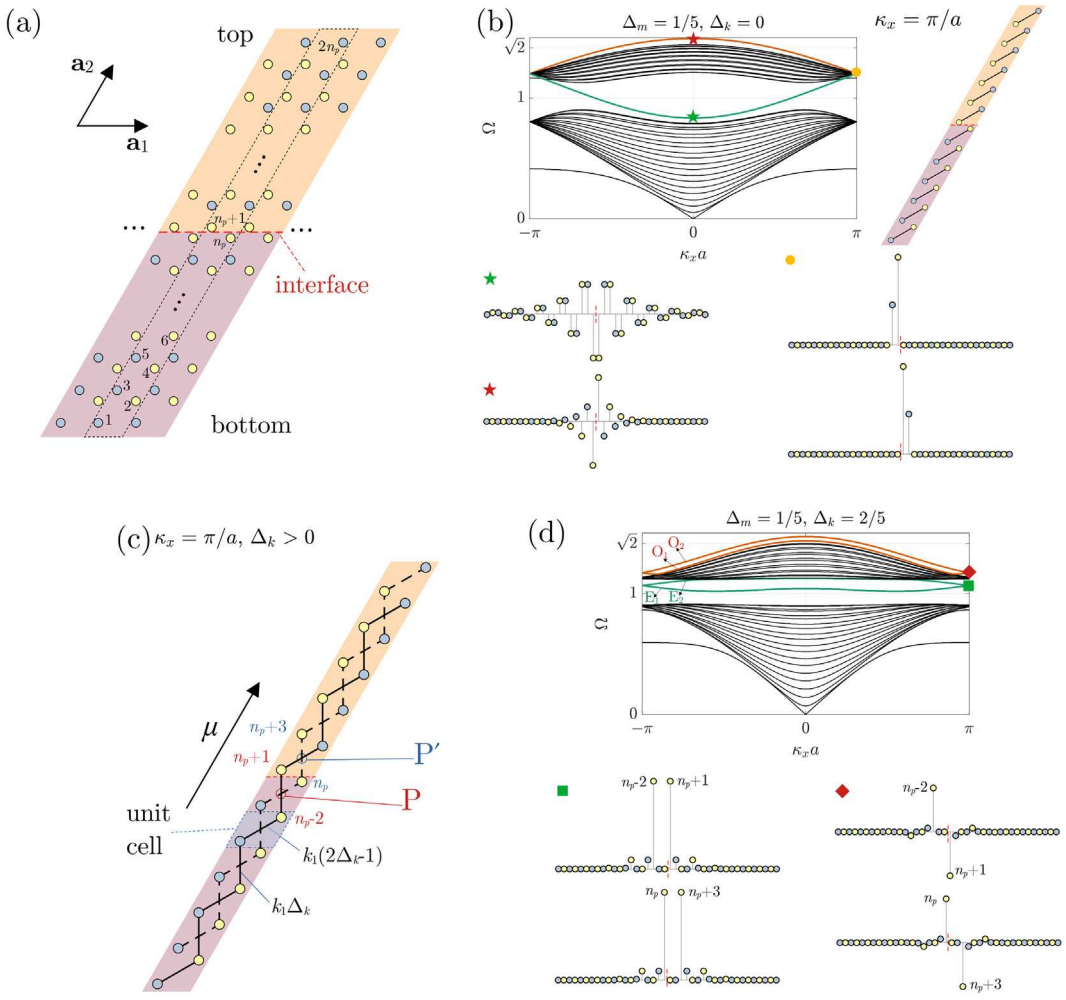

Fig. 3. Dispersion diagrams and localized modes in a finite strip. (a) Lattice with periodicity in the $\mathbf{a}_1$-direction and a finite length in the $\mathbf{a}_2$-direction, presenting an interface between the top ($\Delta_{m,t}$, in orange) and bottom ($\Delta_{m,b} = -\Delta_{m,t}$, in purple) regions. (b) Dispersion curves for $\Delta_m = 1/5$, $\Delta_k = 0$, with branches having even (green) and odd (red) symmetries enveloping the bulk bands, whose wave modes are shown at $\kappa_x = 0$ (green and red starts, respectively). These modes converge to a set of bound modes in the continuum, showing the localized motion of pairs of masses (yellow circle) due to decoupled consecutive unit cells (top right panel). (c) Decoupled pairs of dimer chains at $\kappa_x = \pi/a$ with symmetry at the point P (P′) for the chain marked with continuous (dashed) lines. (d) Dispersion curves computed for $\Delta_m = 1/5$, $\Delta_k = 2/5$. The even (odd) modes indicated as E_1/E_2 (O_1/O_2) and highlighted in green (red) merge into bound modes marked by the green square (red diamond) at $\kappa_x = \pi/a$, who display even (odd) symmetry about the P (P′) point, relative to masses $n_p - 2/n_p + 1$ ($n_p/n_p + 3$).

$\kappa_x = \pi/a$, the strip unit cell decouples into two dimer chains related to the indices $\{1, 2, 5, 6, \dots, n_p+1, n_p+2, \dots, 2n_p-3, 2n_p-2\}$ and $\{2n_p, 2n_p-1, \dots, n_p, n_p-1, \dots, 8, 7, 4, 3\}$. Fig. 3c reports a schematic representation of these unit cells with the resulting dimer chain connections indicated in continuous and dashed black lines, respectively. Since the two chains are identical, a two-fold degeneracy in the set of frequencies at $\kappa_x = \pi/a$ is implied, and their mode shapes $(\mathbf{u}, \mathbf{v})$ to be related as $u_m = v_{2n_p+1-m}$ (m takes values in the first set above). The effective stiffness of springs in the dimer chains, $k_1\Delta_k$ and $k_1(2\Delta_k - 1)$, yield zero-valued stiffness connections for the values of $\Delta_k = 0$ (as previously demonstrated in Fig. 3b) and $\Delta_k = 1/2$, respectively.

Having shown that the strip unit cell decouples into two chains at $\kappa_x = \pi/a$, we now analyze the topological properties of the chains on either side of the interface. The topological properties leading to the presence of localized and bound modes at the interface of these decoupled dimer chains are analyzed by initially considering the dispersion behavior of a unit cell belonging to the bottom domain (dashed parallelogram) in Fig. 3c. Using Bloch–Floquet periodicity conditions, its governing equations at the normalized wavenumber μ reduce to the form $\widetilde{\mathbf{K}}_{\mathrm{X}}\mathbf{u} = \Omega^2\widetilde{\mathbf{M}}_{\mathrm{X}}\mathbf{u}$ with the dimensionless stiffness $\widetilde{\mathbf{K}}_{\mathrm{X}}$ and mass $\widetilde{\mathbf{M}}_{\mathrm{X}}$ matrices given by

$$\widetilde{\mathbf{K}}_{\mathrm{X}} = \mathbf{I}_2 - \frac{2\Delta_k - 1 + \Delta_k\cos\mu}{3(1+\Delta_k)}\sigma_x - \frac{\Delta_k \sin\mu}{3(1+\Delta_k)}\sigma_y\,,$$
$$\widetilde{\mathbf{M}}_{\mathrm{X}} = \mathbf{I}_2 + \Delta_m\sigma_z\,, \tag{16}$$

where $\mathbf{u}$ represents the displacements in a unit cell formed by following masses of index $2n$ and $2n+1$ of the dimer chain, $\mathbf{I}_2$ is an order-2 identity matrix, and σ_i are the set of Pauli matrices. The normalized wavenumber μ measures the periodicity of waves along a_2 on the bottom half of the strip unit cell at $\kappa_x = \pi/a$. An analogous dispersion relation can be obtained for the upper side of the interface by considering $\widetilde{\mathbf{M}}_{\mathrm{X}} = \mathbf{I}_2 - \Delta_m\sigma_z$. Note that this dimer chain becomes identical to the well investigated Su–Schrieffer–Heeger (SSH) chain when $\Delta_m = 0$. However, the results of SSH chain are not applicable here since we do not have an interface in the strip when $\Delta_m = 0$. Similar dimer chains, where both the adjacent masses and adjacent springs are distinct, were considered recently by Liu and Semperlotti [78]. In this work, the authors identified nontrivial topological behavior associated with $\Delta_m < 0$ when all springs are identical and showed the existence of localized modes at the ends of the chain. In contrast, here we have an interface between two lattices, along with both the adjacent spring stiffness and

mass values are different. To investigate its behavior, we observe that the dimer chain obtained for $\kappa_x = \pi/a$ (Fig. 3c) has inversion symmetry about the point P (P′). This point corresponds to the interface between masses $n_p - 2$ and $n_p + 1$ (n_p and $n_p + 3$) for the dimer chain represented using continuous (dashed) lines.

Let us now proceed to investigate the dispersion diagram of the strip for $\Delta_k \neq 0$. We compute the dispersion relations adopting $n_p = 20$, $\Delta_m = 1/5$, and $\Delta_k = 2/5$ and report the corresponding dispersion diagram in the top panel of Fig. 3d. Similarly to the case of $\Delta_k = 0$, the diagram exhibits bulk modes (black lines) and interface modes characterized by even and odd symmetries with respect to the interface, indicated as the green and red lines, respectively. In this case, however, for each symmetry (even or odd) a pair of branches is present, denoted as E_1, E_2 and O_1, O_2, respectively. Approaching $\kappa_x = \pi/a$, the two branches E_1 and E_2 of even mode shapes both move inside the band gap and degenerate at $\kappa_x = \pi/a$ (green square in top panel of Fig. 3d) with a mode shape that is even about P/P′ (green square in bottom panel of Fig. 3d). On the contrary, the two branches O_1 and O_2 of odd mode shapes about P/P′ merge into a degeneracy point above the upper bulk bands at $\kappa_x = \pi/a$ (red diamond in top and bottom panels of Fig. 3d). Note that the frequency shift displayed by these modes at $\kappa_x = \pi/a$ is controlled by the variation of the relative stiffness (Δ_k) between first and third nearest neighboring springs. The merging of these pairs of branches happens for all $\Delta_k > 0$ when $\Delta_m > 0$ and $\Delta_k < 1/2$, while, for $\Delta_m < 0$, the even interface branches lie below the lower bulk band at the edge of the Brillouin zone, while the odd interface branches lie in the band gap.

The inversion symmetry is recognizable from the shown wave modes (bottom panel of Fig. 3d) which indicates the symmetries between the pairs of masses $n_p - 2/n_p + 1$ and $n_p/n_p + 3$. These features arise from the symmetry properties of the interface. The two modes undergo braiding and thus interchange at $\kappa_x = 2\pi/a$. The reason for the two-fold degeneracy at $\kappa_x = \pi/a$ in the dispersion of the strip unit cell derives from the adjacent unit cells moving exactly out-of-phase, which results in a net cancellation of forces between a set of masses. These cancellations effectively decouple the interface unit cell into two chains. Detailed derivations are presented in Appendix D. The strip unit cell has inversion symmetry about a point at its center, i.e., the lattice remains unchanged under the transformation $\mathbf{r} \to -\mathbf{r}$ for the nodal position vector $\mathbf{r}$. This symmetry holds for all wavenumbers κ_x. In addition, at $\kappa_x = \pi/a$, each of the decoupled chains has an additional inversion symmetry. The continuous and dashed chains are symmetric about the points P and P′, respectively.

Explicit expressions for the frequencies and mode shapes of the localized modes in the decoupled chain at $\kappa_x = \pi/a$ are derived to illustrate the topological nature of the transition that results in bound modes. A transfer matrix approach similar to that presented in [79] is used. A harmonic solution of the form $e^{-i\omega t}\mathbf{u}$ is assumed for the decoupled chain with continuous lines. In these expressions, masses are re-labeled starting from the interface using positive integers ($n > 0$) starting from 1 (mass closest to the interface). The governing equations for masses $2n$ and $2n + 1$ (masses more distant from the interface) may then be written (see Appendix D) as

$$\begin{Bmatrix} u_{2n+1} \\ u_{2n+2} \end{Bmatrix} = \begin{bmatrix} (1-2\Delta_k)/\Delta_k & \gamma_+ \\ -\gamma_- & (1-\gamma_+\gamma_-)\Delta_k/(1-2\Delta_k) \end{bmatrix} \begin{Bmatrix} u_{2n-1} \\ u_{2n} \end{Bmatrix}, \tag{17}$$

where $\gamma_\pm = (3(1+\Delta_k) - \omega^2(1 \pm \Delta_m)m/k_1)/\Delta_k$. The 2×2 transfer matrix in the above equation, indicated hereafter by $\mathbf{T}$, is symplectic satisfying the identity $\mathbf{T}^T\mathbf{W}\mathbf{T} = \mathbf{W}$ with $\mathbf{W} = i\sigma_y$ and $\det(\mathbf{T}) = 1$. The two eigenvalues λ of matrix $\mathbf{T}$, obtained from the relation $\mathbf{T}\{u_{2n-1}, u_{2n}\}^T = \lambda\{u_{2n-1}, u_{2n}\}^T$, $n > 0$, are the inverse of each other. Also, applying the above equation successively yields

$$\{u_{2n+1}, u_{2n+2}\}^T = \mathbf{T}^n \{u_1, u_2\}^T, \tag{18}$$

for displacements $\{u_1, u_2\}^T$ of the unit cell located at the interface. For a mode to be localized at the interface, its displacement must decay to zero as $n \to \infty$. The objective now is to obtain modes where $\{u_1, u_2\}^T$ is an eigenvector of $\mathbf{T}$ with an eigenvalue $|\lambda| < 1$, a condition which fulfills the requirement of displacements decaying to zero [80].

The possible choices for displacements $\{u_1, u_2\}^T$ cannot be arbitrary and needs to satisfy the governing equation of the interface mass. Since the chain has reflection symmetry about the interface, its mode shapes are thus eigenvectors of the reflection operator [81]. The eigenvalues of this operator are ± 1, which correspond to even and odd modes about the interface. Eliminating the displacement of the mass across the interface by imposing each of these symmetry conditions, the governing equation for the interface mass becomes

$$(2\Delta_k - 1)\, u_2 = \left(3 + 2\Delta_k - \omega^2(1-\Delta_m)m/k_1\right) u_1, \quad \text{for the even mode,} \tag{19a}$$

$$(2\Delta_k - 1)\, u_2 = \left(3 + 4\Delta_k - \omega^2(1-\Delta_m)m/k_1\right) u_1, \quad \text{for the odd mode.} \tag{19b}$$

From numerical simulations, we observe the relations $u_2 = u_3$ and $u_2 = -u_3$ for the even and odd modes, respectively (see mode shapes in Fig. 4a). Using these relations in Eq. (17) gives the condition

$$T_{11}u_1 + T_{12}u_2 = \pm u_2 \tag{20}$$

where T_{ij} are the components of $\mathbf{T}$, for the even (+) and odd (−) modes, respectively. Substituting Eq. (19) into this condition results in quadratic equations for ω^2 in each case (even, odd). An alternate approach to determine ω is using the eigenvector condition, i.e., $\{u_1, u_2\}^T$ is an eigenvector of $\mathbf{T}$ along with Eq. (19) [79].

The solution of the quadratic equation yields two frequencies in each case, even and odd. To determine if these are valid solutions, we verify that the corresponding eigenvalue of $\mathbf{T}$ satisfies $|\lambda| < 1$. From Eq. (20), we infer that $\lambda u_1 = \pm u_2$ for the even (+) and odd (−) modes, respectively. Substituting this into Eq. (19) gives explicit expressions for λ. Numerical computations showed that $|\lambda| < 1$ for one solution in each of the odd and even cases, i.e., we have two valid solutions for modes localized at the interface. In particular, when $\Delta_m < 0$ ($\Delta_m > 0$), the odd (even) mode lies in the band gap, while the even (odd) mode is outside the lower (upper) bulk band.

The natural frequency Ω_e of the even localized mode, obtained with the above procedure, is given by

$$\Omega_e^2 = \frac{3 + 2\Delta_k + \text{sign}(\Delta_m)\sqrt{(2\Delta_k - 1)^2 + 8(1+2\Delta_k)\Delta_m^2}}{3(1+\Delta_k)(1-\Delta_m^2)}. \tag{21}$$

The corresponding localized mode shape can be expressed in terms of the number n of masses away from the interface in the considered chain using Eq. (18). It is given by

$$\begin{Bmatrix} u_{\pm 2n} \\ u_{\pm(2n+1)} \end{Bmatrix} = \left[\frac{3 + 2\Delta_k - 3\Omega_e^2(1+\Delta_k)(1-\Delta_m)}{2\Delta_k - 1}\right]^{|n|} \begin{Bmatrix} 1 \\ 1 \end{Bmatrix}, \quad n \in \mathbb{N}. \tag{22}$$

Similarly, the natural frequency Ω_o of the odd localized mode is given by

$$\Omega_o^2 = \frac{3 + 4\Delta_k + \text{sign}(\Delta_m)\sqrt{(2\Delta_k - 1)^2 + 4(2+\Delta_k)(1+3\Delta_k)\Delta_m^2}}{3(1+\Delta_k)(1-\Delta_m^2)}, \tag{23}$$

with the corresponding localized mode shape

$$\begin{Bmatrix} u_{\pm 2n} \\ u_{\pm(2n+1)} \end{Bmatrix} = \pm\left[\frac{3 + 4\Delta_k - 3\Omega_o^2(1+\Delta_k)(1-\Delta_m)}{1 - 2\Delta_k}\right]^{|n|} \begin{Bmatrix} -1 \\ 1 \end{Bmatrix}, \quad n \in \mathbb{N}, \tag{24}$$

where u_{+q} (u_{-q}) indicates the displacement of the qth mass on the left (right) side of the interface in Fig. 3c. In this mode shape, the displacement of masses at the interface are set to $u_1 = -u_{-1} = 1$.

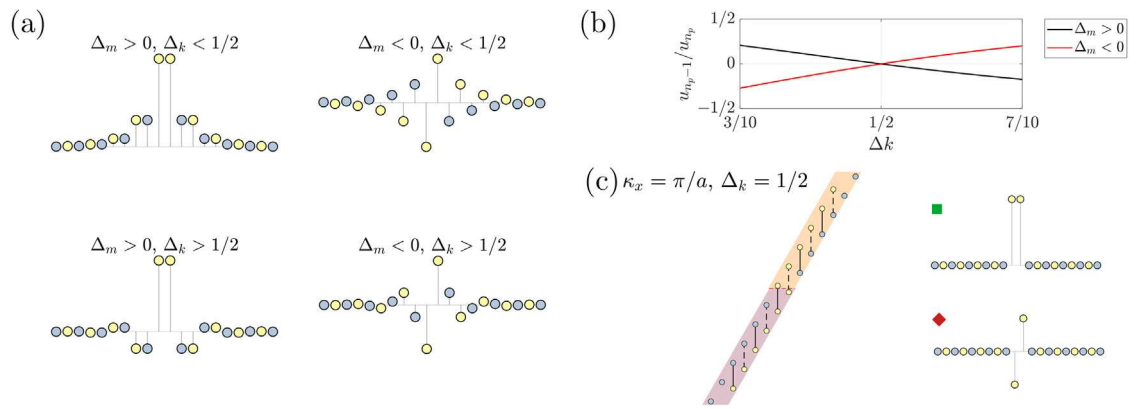

Fig. 4. Localized mode shapes and dimer chain for $\Delta_k = 1/2$. (a) Mode shapes in a decoupled at $\kappa_x = pi/a$ for obtained for $\Delta_m = +1/5 > 0$ (left column), $\Delta_m = -1/5 < 0$ (right column), $\Delta_k = 1/5 < 1/2$ (upper row), and $\Delta_k = 4/5 > 1/2$ (lower row), decay of modes from the interface. (b) Ratio of u_{n_p-1}/u_{n_p} Δ_k transverses the value 1/2 has a transition through zero. (c) Decoupling of masses for $\Delta_k = 1/2$ at the wavenumber $\kappa_x = \pi/a$ showing perfectly isolated bound modes (marked under the green square and red diamond) in the band gap.

Fig. 4a displays the interface localized mode shapes for two values of mass difference, $\Delta_m = \pm 1/5$. For the case $\Delta_m > 0$, the localized modes ($\Delta_m > 0, \Delta_k < 1/2$ and $\Delta_m > 0, \Delta_k > 1/2$) are even about P. It is interesting to note that the sign of the displacement of the blue mass adjacent to the interface changes as Δ_k varies about 1/2, shown here for $\Delta_k = 1/5$ and 4/5. Since the mode shapes change continuously as Δ_k is varied between these values, it indicates that the blue mass has zero displacement for at least one value of Δ_k in this interval. To investigate this observation, the variation of the ratio of displacements of the blue and the yellow masses (u_{n_p-1} and u_{n_p}, respectively) considering the wave mode in the band gap is shown in Fig. 4b for values of Δ_k in the vicinity of 1/2. For both $\Delta_m = +1/5 > 0$ and $\Delta_m = -1/5 < 0$, we have a zero ratio of displacements at $\Delta_k = 1/2$.

It is interesting to recall that the case $\Delta_k = 1/2$ implies a zero stiffness for the internal connections of the dimer chain (see Fig. 3c), resulting in the effective decoupling indicated in Fig. 3g (top panel). In this case, each wave mode at the edge of the first Brillouin zone is associated with specific pairs of masses. The resulting bound modes corresponding to the even and odd mode shapes for this case are shown in Fig. 4c (top and bottom rows of the right panel, respectively). At this Δ_k value, from the mode shape expression in Eq. (22), we notice that the decay factor must go to zero to satisfy $\{u_1, u_2\}^T = \{1, 0\}^T$. Thus, all other masses away from the interface will also have zero displacement. A similar argument indicates the existence of a bound mode in the $\Delta_m < 0$ case, shown by the odd mode shapes in Fig. 4a ($\Delta_m < 0, \Delta_k < 1/2$ and $\Delta_m < 0, \Delta_k > 1/2$). We mention here that this decoupling is similar to the one obtained in the case of $\Delta_k = 0$. However, when $\Delta_k = 1/2$, the frequencies of the resulting pairs of bound modes lie in the band gap, making it easier to excite and thus exploit them in practical applications. This tunability of the frequencies in which bound modes appear is enabled by the additional designing degree of freedom added by the third nearest neighbor connections.

Furthermore, by varying the stiffness of the nonlocal springs in the direction normal to the interface (vertical dashed lines), the odd bound mode frequency can be shifted to an arbitrary value above a threshold. Indeed, let k_v be the stiffness of springs indicated by dashed lines pointing in the $(0, 1)$ direction in Fig. 1a. The decoupling of masses illustrated in Fig. 4c is valid under this stiffness change, with the connecting springs now having value $k_1 \Delta_v$. The odd bound mode frequency Ω_o then becomes

$$\Omega_o^2 = \frac{4\left(2 + \Delta_v\right)}{9\left(1 - \text{sign}(\Delta_m)\Delta_m\right)}. \tag{25}$$

By varying Δ_v, the frequency Ω_o can take an arbitrary value above a minimum threshold value when $\Delta_v = 0$. This minimum value is equal to the frequency Ω_e of the even bound mode shape.

For the sake of completeness, the behavior of the strip is also analyzed for $\kappa_x = 0$. In this case, the resulting strip unit cell becomes a dimer chain with distinct adjacent masses and springs, along with an interface having identical adjacent masses. In contrast to the case $\kappa_x = \pi/a$, the dimer chain here has non-neighboring connections and three distinct spring stiffness values $2k_1$, $k_1(1 + 2\Delta_k)$, and $k_1\Delta_k$ (see Appendix D). The analysis of the wave propagation along the strip yields the normalized stiffness and mass matrices of a unit cell given by

$$\begin{aligned} \widetilde{\mathbf{K}}_0 &= \mathbf{I}_2 - \frac{2 + (1 + 3\Delta_k)\cos\mu}{3(1 + \Delta_k)}\sigma_x - \frac{\sin\mu}{3}\sigma_y, \\ \widetilde{\mathbf{M}}_0 &= \mathbf{I}_2 \pm \Delta_m \sigma_z, \end{aligned} \tag{26}$$

where the $\pm$ sign is for the mass matrix at the bottom and top regions.

The eigenproblem stated as $\widetilde{\mathbf{K}}_0\mathbf{u} = \Omega^2\widetilde{\mathbf{M}}_0\mathbf{u}$ yields the dispersion relation associated with the lower and upper bulk bands at $\kappa_x = 0$, as shown in Fig. 3b. The band gap region at $\kappa_x = 0$ is thus delimited by the frequencies obtained at $\mu = \pi$ and given by

$$\Omega_b^2 = \frac{1}{1 - \Delta_m^2}\left(1 \pm \sqrt{1 - (1 - \Delta_m^2)\left(1 - \left(\frac{3\Delta_k - 1}{3\Delta_k + 3}\right)^2\right)}\right), \tag{27}$$

which represent the propagating frequencies at the superior edge of the bulk band with lower frequencies (−) and inferior edge of the bulk band with higher frequencies (+).

For the case $\Delta_m > 0$, we numerically observe (see Supplementary Movie 2) that the band gap present among these bulk bands contains one even wave mode localized at the interface, which is located close to the superior edge of the lower bulk band, for $\Delta_k = 0$, and crosses the band gap until the inferior edge of the upper bulk band, for $\Delta_k \gg 1$. When $\Delta_m < 0$, an odd mode appears within the band gap, crossing the band gap from the upper to the lower bulk bands.

5. Numerical results

5.1. Numerical results on a finite lattice

Numerical examples considering a finite structure containing a "Z"-shaped interface are now presented to verify the exploitation of bound modes in a waveguiding application. To this end, a finite structure comprised of 60 × 40 unit cells (see Fig. 5a) with third nearest neighboring masses connected as the one reported in Fig. 1a is considered. The value $\Delta_m = 1/2$ is selected, thus yielding even bound modes with a frequency of $\Omega_e = 4/3$ (see Eq. (21)).

An eigenmode analysis is initially performed for the cases $\Delta_k = 0$ and $\Delta_k = 1/2$ to verify the existence of interface modes at resonant

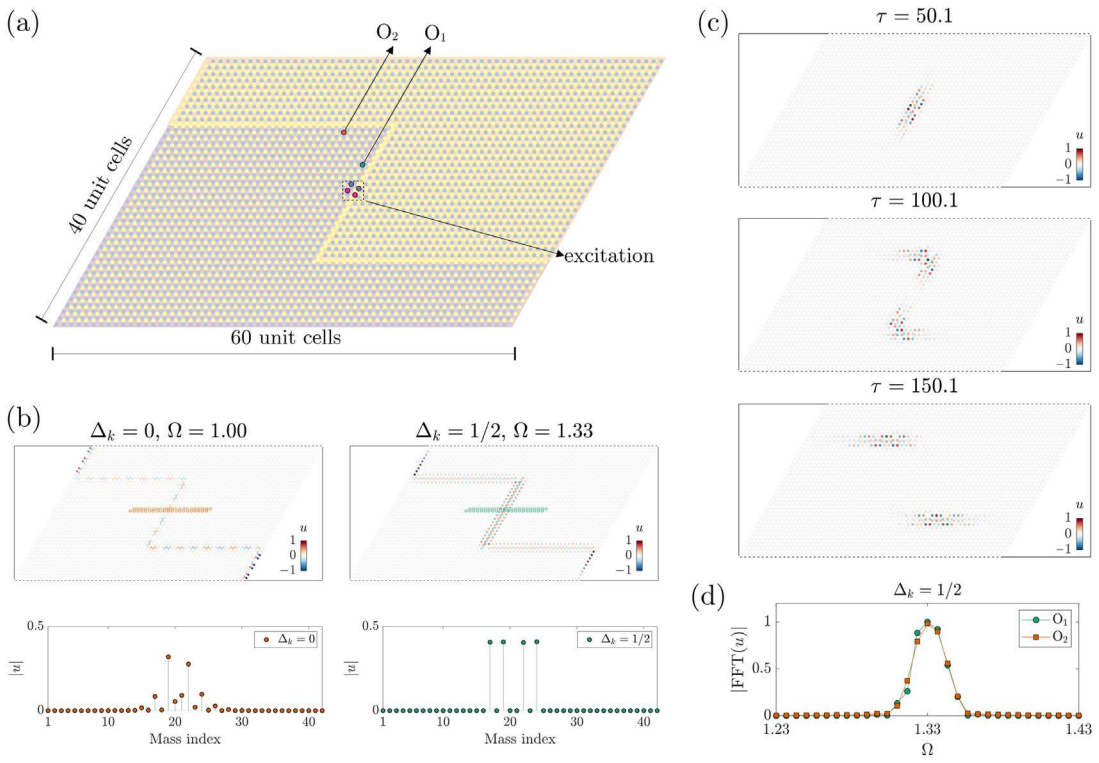

Fig. 5. Waveguiding application for propagation along sharp corners. (a) Finite structure (60 × 40 unit cells) presenting a "Z" interface between distinct regions. The pair of nodes shown in purple and pink ("excitation") are excited, and the displacements of the masses labeled as O_1 and O_2 (before and after the corner, respectively) are used as outputs for the FFT computation. (b) Example of vibration modes for $\Delta_m = 1/2$ obtained at $\Omega_t = 1$ for $\Delta_k = 0$ (top left) and $\Omega_e = 4/3$ for $\Delta_k = 1/2$ (top right). The displacement profiles along the highlighted 21 pairs of masses for each case (in red and green, respectively) are shown in the bottom panels. (c) Transient analysis results for $\Delta_k = 1/2$ at the time instants $\tau = 50.1$, 100.1, and 150.1. (d) FFT applied to the transient response considering the displacements of the masses labeled as O_1 and O_2 (before and after the sharp corner, respectively).

frequencies of interest. Free boundary conditions are considered at all edges of the finite structure. Our numerical results indicate the existence of 7 vibration modes in the frequency range $\Omega_t \pm 0.01$, $\Omega_t = 1$ (center of the band gap), for the case $\Delta_k = 0$, whereas 10 vibration modes are obtained for the case $\Delta_k = 1/2$ in the frequency range $\Omega_e \pm 0.01$. The vibration modes with the values closest to Ω_t and Ω_e, for $\Delta_k = 0$ and $\Delta_k = 1/2$, are shown in the top left and right panels of Fig. 5b, respectively. We notice (i) a phase inversion of subsequent unit cells and (ii) a better localization of displacements of masses adjacent to the interface for $\Delta_k = 1/2$ when compared to $\Delta_k = 0$. To verify these observations, we also plot the displacements of the 21 pairs of masses highlighted in red ($\Delta_k = 0$) and green ($\Delta_k = 1/2$). Both displacement profiles are shown in the bottom panel of Fig. 5b, indicating an ideal localization of two pairs of masses for the case $\Delta_k = 1/2$.

Next, a transient analysis in the time domain is performed to verify the propagation of elastic waves along the interface for the case $\Delta_k = 1/2$. The transient analysis is performed considering a total of $\tau = 200$ fundamental periods ($2\pi/\Omega_e$). A sinusoidal signal with the central frequency Ω_e is applied for $\tau \in [0, 100]$ modulated by a Hanning window to achieve a narrowband excitation. This signal is applied in the form of forces with alternating signs for subsequent pairs of masses (purple and pink circles, marked as "excitation" in Fig. 5a). The Newmark method is employed with 2^{11} time steps [82].

The displacement fields obtained in the transient analysis are represented in Fig. 5c, with increasing values of time instants from top to bottom ($\tau = 50.1$, 100.1, and 150.1). The displacement values for the three distinct time instants are normalized for a better visualization.

It is interesting to notice that the excitation of bound modes can easily be observed, staying mostly confined to the pair of masses that were excited. Some residual excitation of masses other than the selected two pairs can also be noticed due to the existence of frequency components slightly different from Ω_e in the time signal. Furthermore, it is also important to notice that due to the topological nature of the excited modes, the energy is able to propagate along the sharp corners (see $\tau = 150.1$) with negligible backscattering, thus indicating the localized waveguiding capabilities achieved for the configuration $\Delta_k = 1/2$.

This observation is further verified by performing a fast Fourier transform (FFT) on the displacements of selected masses with locations before and after the sharp corner (masses labeled as O_1 and O_2, marked in green and red, respectively, in Fig. 5a). The resulting FFT, shown in Fig. 5d, demonstrates a clear concentration of energy around $\Omega_e = 4/3$ for both cases, with a comparable level of frequency components between both cases, thus indicating the efficiency of this structure for waveguiding applications.

5.2. Elastic unit cell with third nearest neighbor couplings

Envisaging the experimental validation of the concepts arising from nonlocal interactions presented in this work, we also propose here a possible realization of a hexagonal unit cell with third nearest neighbor connections. A schematic representing the corresponding lattice is presented in Fig. 6a, where a parallelogram denoting a unit cell with lattice constant a is highlighted by the dashed lines, and the mass elements are represented in blue and light yellow. Elements performing nearest neighbor connections, with length $l_1 = a\sqrt{3}/3$, are represented in gray, and elements connecting third nearest neighbors, with length $l_2 = 2a\sqrt{3}/3$, are represented in purple, green, and orange, respectively.

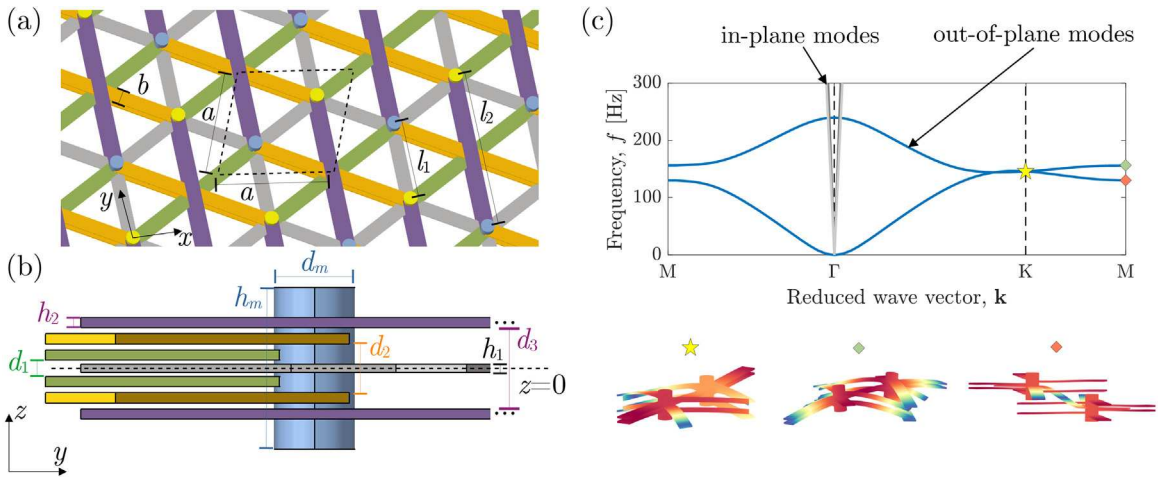

Fig. 6. Unit cell design for a potential experimental realization. (a) Proposed lattice with unit cell of length a (parallelogram with dashed lines) containing nearest (in gray, length l_1) and third nearest neighbor connection elements (in purple, green, and orange, length l_2) having a width b. (b) Portion of the unit cell where the ideal mass is implemented as a cylinder of diameter d_m and height h_m; nearest (third nearest) neighbor connection elements have a thickness h_1 (h_2); the distance between each pair of non-nearest connections is given by d_1 (green), d_2 (orange), and d_3 (purple). (c) Example of associated dispersion diagram. In-plane modes are marked using gray lines, and out-of-plane modes are marked using blue lines. The dominant flexural behavior is illustrated by the wave modes obtained at the K and M points (represented using the yellow star and red/green diamonds, respectively).

All connecting elements present the same width b. The third nearest neighbor connection elements do not interact with each other due to a disalignment imposed between them in the z direction.

Details on the z-coordinate of connection elements are shown in Fig. 6b, which shows a portion of the unit cell in the yz plane. The mass elements (blue and light yellow) are modeled as cylinders with a height h_m and diameter d_m, thus allowing the unit cell symmetry to be manipulated by modulating h_m, which may assume different values for the two masses. Elements performing the nearest (third nearest) neighbor connections have a thickness h_1 (h_2). Elements associated with the third nearest neighbor connections are included in pairs, symmetrically with respect to the xy plane and coordinate $z = 0$ (midsurface of gray elements), at different heights d_1 (green elements, $d_1 > h_1$), d_2 (orange elements), and d_3 (purple elements, $d_3 < h_m - 2h_2$). The pairing of these elements is imposed to ensure symmetry with respect to the xy-plane and avoid the coupling between in-plane and out-of-plane motion. The condition of non-interference between third nearest neighbor elements is ensured by $(d_2 - d_1)/2 > h_2$ and $(d_3 - d_2)/2 > h_2$. The ratio between the stiffness of beams which approximate the behavior of nearest (k_1) and third nearest (k_2) neighbor elements is theoretically controlled by the ratio between their thickness according to $k_2/k_1 = (1/4)(h_2/h_1)^3$.

The dispersion relation of the proposed structure can be computed with the use of finite element analysis, enforcing periodic boundary conditions at opposing edges of the hexagonal unit cell [18]. As an example, we consider the following geometrical dimensions: $a = 20$ mm, $h_m = 0.2a$, $d_m = 0.1a$, $b = 0.1a$, $h_1 = 0.01a$, $h_2 = h_1 2^{1/3}$, $d_1 = 0.02a$, $d_2 = 0.06a$, $d_3 = 0.10a$, and material properties: Young's modulus $E = 1$ GPa, Poisson's ratio $\nu = 0.3$, and specific mass density $\rho = 2000$ kg/m^3. The obtained unit cell is meshed using tetrahedral quadratic solid elements. The dispersion diagram (see Fig. 6c) shows a decoupling between in-plane modes (gray lines) and out-of-plane modes (blue lines). The wave modes indicated at the high-symmetry points K and M (marked using the yellow star and red/green diamonds, respectively) illustrate the behavior of the unit cell, which propagates flexural waves. Although these results are preliminary, and additional adjusting must be implemented due to the considerably more complex interactions arising at the connections of solid elements, which therefore deviate from the ideal $\Delta_k = 1/2$ condition, these results are indicative of the feasibility of experimental realization for the observation of the phenomena described in this work.

6. Conclusions

In conclusion, the topological-related dynamics of a mass–spring hexagonal lattice with springs connecting both nearest and third nearest neighboring masses has been investigated. The formation and evolution in the reciprocal space of multiple Dirac cones as the relative stiffness between the two sets of springs (connecting the nearest and third nearest masses) is changed has been highlighted. Specifically, the nucleation of Dirac cones at the M-points have been shown for $\Delta_k = 1/3$, following their merging at the K-points for $\Delta_k = 1/2$. It has also been found that the multiplicity of Dirac cones remains for $\Delta_k > 1/2$. The computation of the Berry flux for different values of Δ_k has elucidated opposite valley Chern numbers for the aforementioned cones.

The increase in the number of Dirac cones has been shown to lead to a corresponding increase in the number of topological edge modes hybridizing and leading to bound modes (i.e., modes ideally capable of perfect spatial wave confinement) when finite strips are considered due to symmetry conditions producing a pair of decoupled linear dimer chains. First observed in the case of only nearest neighbor connections ($\Delta_k = 0$), these bound modes were found to be trapped in a frequency region of bulk modes (revealing, thus, a bound mode in the continuum). Second, connecting the third nearest neighboring masses in the hexagonal lattice has enabled a frequency shift of the aforementioned bound modes isolating them inside a frequency band gap. Third, by varying the stiffness the nonlocal springs normal to the interface, the odd bound mode frequency can be shifted to an arbitrary value above a threshold. The existence of these bound modes is guaranteed by topological arguments, as the adjacent masses transition from moving in-phase to out-of-phase across the critical $\Delta_k = 1/2$ value. Explicit expressions have been given for the existence of localized modes at the interface and their topological origin elucidated.

Finally, numerical simulations on a finite lattice have been conducted to determine the extent of the confinement along the transverse direction as a wave propagates in a waveguide with sharp turns. The frequency contents presented by the displacements of masses before

and after the sharp corners, obtained using a transient analysis, has suggested a negligible backstattering effect for the case $\Delta_k = 1/2$. A unit cell considering a solid three-dimensional model was also proposed and its experimental realization will be part of a future publication.

The concepts presented here using discrete elements can be extended to continuous systems which leverage bound modes to design waveguides with superior energy localization.

CRediT authorship contribution statement

V.F. Dal Poggetto: Writing – review & editing, Writing – original draft, Software, Methodology, Investigation, Formal analysis, Data curation, Conceptualization, Visualization. **R.K. Pal:** Writing – original draft, Software, Methodology, Investigation, Formal analysis, Conceptualization. **N.M. Pugno:** Writing – review & editing, Funding acquisition, Conceptualization. **M. Miniaci:** Writing – review & editing, Writing – original draft, Supervision, Resources, Project administration, Conceptualization, Visualization, Funding acquisition.

Declaration of competing interest

The authors declare that they have no known competing financial interests or personal relationships that could have appeared to influence the work reported in this paper.

Data availability

Data will be made available on request.

Acknowledgments

VFDP and MM are supported by the European Union's Horizon Europe programme in the framework of the ERC StG POSEIDON under Grant Agreement No. 101039576. RKP is supported by the U.S. National Science Foundation under Award No. 2027455.

Supplementary material

Supplementary material related to this article can be found online at https://doi.org/10.1016/j.ijmecsci.2024.109503.

References

[1] Kaplunov JD, Rogerson GA, Tovstik PE. Localized vibration in elastic structures with slowly varying thickness. Quart J Mech Appl Math 2005;58(4):645–64.
[2] Zalipaev VV, Movchan AB, Jones IS. Waves in lattices with imperfect junctions and localized defect modes. Proc R Soc A 2008;464(2096):2037–54.
[3] Craster RV, Kaplunov J, Postnova J. High-frequency asymptotics, homogenisation and localisation for lattices. Quart J Mech Appl Math 2010;63(4):497–519.
[4] Fu YB, Kaplunov J. Analysis of localized edge vibrations of cylindrical shells using the Stroh formalism. Math Mech Solids 2012;17(1):59–66.
[5] Pagneux V. Complex resonance and localized vibrations at the edge of a semi-infinite elastic cylinder. Math Mech Solids 2012;17(1):17–26.
[6] Zangeneh-Nejad F, Alù A, Fleury R. Topological wave insulators: a review. C R Phys 2020;21(4–5):467–99.
[7] Khanikaev AB, Alù A. Topological photonics: robustness and beyond. Nat Commun 2024;15(1):931.
[8] Laude V. Principles and properties of phononic crystal waveguides. APL Mater 2021;9(8).
[9] Farhat M, Guenneau S, Enoch S. Ultrabroadband elastic cloaking in thin plates. Phys Rev Lett 2009;103(2):024301.
[10] Chaplain GJ, De Ponti JM, Aguzzi G, Colombi A, Craster RV. Topological rainbow trapping for elastic energy harvesting in graded Su-Schrieffer-Heeger systems. Phys Rev Appl 2020;14(5):054035.
[11] Lu L, Joannopoulos JD, Soljačić M. Topological photonics. Nat Photonics 2014;8(11):821–9.
[12] Xue H, Yang Y, Zhang B. Topological acoustics. Nat Rev Mater 2022;7(12):974–90.
[13] Xia B-Z, Liu T-T, Huang G-L, Dai H-Q, Jiao J-R, Zang X-G, et al. Topological phononic insulator with robust pseudospin-dependent transport. Phys Rev B 2017;96(9):094106.
[14] Jin Y, Torrent D, Djafari-Rouhani B. Robustness of conventional and topologically protected edge states in phononic crystal plates. Phys Rev B 2018;98(5):054307.
[15] Hasan MZ, Kane CL. Colloquium: topological insulators. Rev Modern Phys 2010;82(4):3045.
[16] Zárate Y, Babaee S, Kang SH, Neshev DN, Shadrivov IV, Bertoldi K, et al. Elastic metamaterials for tuning circular polarization of electromagnetic waves. Sci Rep 2016;6(1):28273.
[17] Ma G, Fu C, Wang G, Del Hougne P, Christensen J, Lai Y, et al. Polarization bandgaps and fluid-like elasticity in fully solid elastic metamaterials. Nat Commun 2016;7(1):13536.
[18] Dal Poggetto VF, Bosia F, Miniaci M, Pugno NM. Band gap enhancement in periodic frames using hierarchical structures. Int J Solids Struct 2021;216:68–82.
[19] Rui S, Zhang W, Yu R, Wang X, Ma F. A multi-band elastic metamaterial for low-frequency multi-polarization vibration absorption. Mech Syst Signal Process 2024;216:111464.
[20] Ma G, Sheng P. Acoustic metamaterials: From local resonances to broad horizons. Sci Adv 2016;2(2):e1501595.
[21] Wu L, Wang Y, Chuang K, Wu F, Wang Q, Lin W, et al. A brief review of dynamic mechanical metamaterials for mechanical energy manipulation. Mater Today 2021;44:168–93.
[22] Gao N, Zhang Z, Deng J, Guo X, Cheng B, Hou H. Acoustic metamaterials for noise reduction: a review. Adv Mater Technol 2022;7(6):2100698.
[23] Craster RV, Guenneau SR, Muamer K, Wegener M. Mechanical metamaterials. Rep Progr Phys 2023.
[24] Miniaci M, Pal R, Morvan B, Ruzzene M. Experimental observation of topologically protected helical edge modes in patterned elastic plates. Phys Rev X 2018;8(3):031074.
[25] Wang G, Chen Z, Shi Z, Lim C. Three-dimensional acoustic metamaterials with topological states of different orders and multidirectional waveguiding. Phys Rev B 2024;109(14):144307.
[26] Morvaridi M, Bosia F, Brun M, Dal Poggetto V, Gliozzi A, Miniaci M, et al. Tunable topologically protected waveguiding in auxetic nonlinear metamaterials. Phys Rev Appl 2024;21:034024.
[27] Nash LM, Kleckner D, Read A, Vitelli V, Turner AM, Irvine WT. Topological mechanics of gyroscopic metamaterials. Proc Natl Acad Sci 2015;112(47):14495–500.
[28] Wang P, Lu L, Bertoldi K. Topological phononic crystals with one-way elastic edge waves. Phys Rev Lett 2015;115(10):104302.
[29] Souslov A, Van Zuiden BC, Bartolo D, Vitelli V. Topological sound in active-liquid metamaterials. Nat Phys 2017;13(11):1091–4.
[30] Ma G, Xiao M, Chan CT. Topological phases in acoustic and mechanical systems. Nat Rev Phys 2019;1(4):281–94.
[31] Miniaci M, Pal R. Design of topological elastic waveguides. J Appl Phys 2021;130(14).
[32] Kane CL, Lubensky TC. Topological boundary modes in isostatic lattices. Nat Phys 2014;10(1):39–45.
[33] Rocklin DZ, Chen BG-g, Falk M, Vitelli V, Lubensky T. Mechanical Weyl modes in topological Maxwell lattices. Phys Rev Lett 2016;116(13):135503.
[34] Kane CL, Mele EJ. Quantum spin Hall effect in graphene. Phys Rev Lett 2005;95(22):226801.
[35] Mousavi SH, Khanikaev AB, Wang Z. Topologically protected elastic waves in phononic metamaterials. Nature Commun 2015;6(1):1–7.
[36] He C, Ni X, Ge H, Sun X-C, Chen Y-B, Lu M-H, et al. Acoustic topological insulator and robust one-way sound transport. Nat Phys 2016;12(12):1124–9.
[37] Chen H, Nassar H, Norris AN, Hu G, Huang G. Elastic quantum spin Hall effect in kagome lattices. Phys Rev B 2018;98(9):094302.
[38] Süsstrunk R, Huber SD. Observation of phononic helical edge states in a mechanical topological insulator. Science 2015;349(6243):47–50.
[39] Pal RK, Schaeffer M, Ruzzene M. Helical edge states and topological phase transitions in phononic systems using bi-layered lattices. J Appl Phys 2016;119(8).
[40] Lu J, Qiu C, Ye L, Fan X, Ke M, Zhang F, et al. Observation of topological valley transport of sound in sonic crystals. Nat Phys 2017;13(4):369–74.
[41] Du Z, Chen H, Huang G. Optimal quantum valley Hall insulators by rationally engineering Berry curvature and band structure. J Mech Phys Solids 2020;135:103784.
[42] Al Ba'ba'a H, Yu K, Wang Q. Elastically-supported lattices for tunable mechanical topological insulators. Extreme Mech Lett 2020;38:100758.
[43] Zhou W, Su Y, Chen W, Lim C, et al. Voltage-controlled quantum valley Hall effect in dielectric membrane-type acoustic metamaterials. Int J Mech Sci 2020;172:105368.
[44] Vila J, Pal RK, Ruzzene M. Observation of topological valley modes in an elastic hexagonal lattice. Phys Rev B 2017;96(13):134307.
[45] Pal RK, Ruzzene M. Edge waves in plates with resonators: an elastic analogue of the quantum valley Hall effect. New J Phys 2017;19(2):025001.
[46] Chen H, Nassar H, Huang G. A study of topological effects in 1D and 2D mechanical lattices. J Mech Phys Solids 2018;117:22–36.
[47] Zhou Y, Bandaru PR, Sievenpiper DF. Quantum-spin-Hall topological insulator in a spring-mass system. New J Phys 2018;20(12):123011.

[48] Chen Y, Liu X, Hu G. Topological phase transition in mechanical honeycomb lattice. J Mech Phys Solids 2019;122:54–68.
[49] An S, Liu T, Fan H, Gao H, Gu Z, Liang S, et al. Second-order elastic topological insulator with valley-selective corner states. Int J Mech Sci 2022;224:107337.
[50] Bulgakov EN, Sadreev AF. Bound states in the continuum in photonic waveguides inspired by defects. Phys Rev B 2008;78(7):075105.
[51] Marinica DC, Borisov AG, Shabanov SV. Bound states in the continuum in photonics. Phys Rev Lett 2008;100(18):183902.
[52] Ndangali RF, Shabanov SV. Electromagnetic bound states in the radiation continuum for periodic double arrays of subwavelength dielectric cylinders. J Math Phys 2010;51(10).
[53] Plotnik Y, Peleg O, Dreisow F, Heinrich M, Nolte S, Szameit A, et al. Experimental observation of optical bound states in the continuum. Phys Rev Lett 2011;107(18):183901.
[54] Hsu CW, Zhen B, Stone AD, Joannopoulos JD, Soljačić M. Bound states in the continuum. Nat Rev Mater 2016;1(9):1–13.
[55] Rahman A, Pal RK. Bound modes in the continuum based phononic waveguides. J Appl Phys 2022;132(11).
[56] Rahman A, Pal RK. Elastic bound modes in the continuum in architected beams. Phys Rev Appl 2024;21(2):024002.
[57] Cao L, Zhu Y, Xu Y, Fan S-W, Yang Z, Assouar B. Elastic bound state in the continuum with perfect mode conversion. J Mech Phys Solids 2021;154:104502.
[58] Cao L, Zhu Y, Wan S, Zeng Y, Li Y, Assouar B. Perfect absorption of flexural waves induced by bound state in the continuum. Extreme Mech Lett 2021;47:101364.
[59] Haq O, Shabanov S. Bound states in the continuum in elasticity. Wave Motion 2021;103:102718.
[60] Chen Y, Kadic M, Wegener M. Roton-like acoustical dispersion relations in 3D metamaterials. Nature Commun 2021;12(1):3278.
[61] Iglesias Martínez JA, Groß MF, Chen Y, Frenzel T, Laude V, Kadic M, et al. Experimental observation of roton-like dispersion relations in metamaterials. Sci Adv 2021;7(49):eabm2189.
[62] Wang K, Chen Y, Kadic M, Wang C, Wegener M. Nonlocal interaction engineering of 2D roton-like dispersion relations in acoustic and mechanical metamaterials. Commun Mater 2022;3(1):35.
[63] Zhu Z, Gao Z, Liu G-G, Ge Y, Wang Y, Xi X, et al. Observation of multiple rotons and multidirectional roton-like dispersion relations in acoustic metamaterials. New J Phys 2022;24(12):123019.
[64] Rajabpoor Alisepahi A, Sarkar S, Sun K, Ma J. Breakdown of conventional winding number calculation in one-dimensional lattices with interactions beyond nearest neighbors. Commun Phys 2023;6(1):334.
[65] Grundmann M. Topological states due to third-neighbor coupling in diatomic linear elastic chains. Phys Status Solidi b 2020;257(9):2000176.
[66] Betancur-Ocampo Y, Manjarrez-Montañez B, Martínez-Argüello A, Méndez-Sánchez RA. Twofold topological phase transitions induced by third-nearest-neighbor hoppings in one-dimensional chains. Phys Rev B 2024;109(10):104111.
[67] Wang S, Wang Y-Z. Nonlocal topological states in elastic wave metamaterials with active feedback control. Int J Solids Struct 2023;281:112430.
[68] Wang S, Wang Y-Z. Active control on topological interface states of elastic wave metamaterials with double coupled chains. J Acoust Soc Am 2023;154(4):2440–52.
[69] Bloch F. Über die Quantenmechanik der Elektronen in Kristallgittern. Z Phys 1929;52(7–8):555–600.
[70] Maurin F, Claeys C, Deckers E, Desmet W. Probability that a band-gap extremum is located on the irreducible Brillouin-zone contour for the 17 different plane crystallographic lattices. Int J Solids Struct 2018;135:26–36.
[71] Brillouin L. Wave propagation in periodic structures: Electric filters and crystal lattices. In: Chemische reihe. lehrbucher und monographien aus dem gebiete der exakten wissenschaften, Dover Publications; 1953.
[72] Zak J. Berry's phase for energy bands in solids. Phys Rev Lett 1989;62(23):2747.
[73] Hasan MZ. Berry's phase and quantization in topological insulators. Physics 2010;3:62.
[74] Fruchart M, Carpentier D. An introduction to topological insulators. C R Phys 2013;14(9–10):779–815.
[75] Zhang F, MacDonald AH, Mele EJ. Valley Chern numbers and boundary modes in gapped bilayer graphene. Proc Natl Acad Sci 2013;110(26):10546–51.
[76] Ozdemir R, Lin J. A rigorous mathematical theory for topological phases and edge modes in spring-mass mechanical systems. Proc R Soc A 2024;480(2287):20230910.
[77] Chen Y, Liu D, Wu Y, Yu P, Liu Y. Valley Hall elastic topological insulator with large Chern numbers. Int J Mech Sci 2023;239:107884.
[78] Liu T-W, Semperlotti F. Classical analogue to the Kitaev model and Majorana-like topological bound states. Phys Rev Appl 2023;20(1):014019.
[79] Pal RK, Vila J, Leamy M, Ruzzene M. Amplitude-dependent topological edge states in nonlinear phononic lattices. Phys Rev E 2018;97(3):032209.
[80] Mencik J-M. On the low-and mid-frequency forced response of elastic structures using wave finite elements with one-dimensional propagation. Comput Struct 2010;88(11–12):674–89.
[81] Dresselhaus MS, Dresselhaus G, Jorio A. Group theory: Application to the physics of condensed matter. Springer Science & Business Media; 2007.
[82] Noh G, Bathe K-J. For direct time integrations: A comparison of the Newmark and ρ_{∞}-Bathe schemes. Comput Struct 2019;225:106079.